Quantitative imaging of nitric oxide concentration in a turbulent n-heptane spray flame

Irfan Mulla, Gilles Godard, Gilles Cabot, Frederic Grisch, Bruno Renou

Version of Record: https://www.sciencedirect.com/science/article/pii/S001021801930063X
Manuscript_81700f553a01d1a1e48f6652a5b8c1eb

Quantitative imaging of nitric oxide concentration in a turbulent *n*-heptane spray flame

I.A. Mulla, G. Godard, G. Cabot, F. Grisch, B. Renou*

Normandie Univ., UNIROUEN, INSA Rouen, CNRS, CORIA, 76000 Rouen, France

Abstract

The present work reports quantitative planar imaging of Nitric Oxide (NO) concentration in a dilute spray flame at atmospheric pressure, contributing to CORIA Rouen Spray Burner (CRSB) database. Mean NO mole fraction (χ_{NO}) is measured using planar laser-induced fluorescence (PLIF) technique, while the flame front is located simultaneously using OH-PLIF. An optimum NO excitation scheme is selected to minimize temperature-quenching dependence based on LIF simulations. Furthermore, the temperature and collisional quenching effects on NO fluorescence are corrected by using the temperature and gas composition obtained from large eddy simulation performed in previous work [Proc. Combust. Inst., 36 (2017), 2567-2575]. Additionally, interferences in NO-PLIF from polycyclic aromatic or unburned hydrocarbon fluorescence is corrected by detuned (NO off-transition) signal subtraction. The spatial distribution of χ_{NO} is discussed in the context of a spray flame topology, which exhibits two distinct branches. The results suggest the formation of prompt NO on the inner composite branch (fuel-lean

*Corresponding author:
Email address: bruno.renou@coria.fr (B. Renou)

and non-premixed) and thermal NO on the outer pure non-premixed branch. χ_{NO} at 60 mm height above burner measures 33 *ppm* near the inner branch, and 75 *ppm* around the outer branch.

Keywords:

Laser-induced fluorescence, Spray combustion, *n*-heptane, NO_x, Nitric oxide

1. Introduction

Combustion of liquid-fueled sprays is of considerable significance to a wide range of practical applications such as furnaces, diesel and gasoline direct injection (GDI) engines, gas turbines, and rocket engines. The spray combustion is also accompanied by unwanted pollutants. In particular, nitric oxide (NO) is one of the primary pollutants produced during the combustion process. To reduce NO_x, it is necessary to understand the NO formation mechanisms. The experimental inputs (database and physical insights) can enhance the model prediction capabilities.

Though numerous studies have reported NO measurements, relatively few have provided the quantitative data. Some of the quantitative works mainly focused on the validation of NO reaction mechanisms by comparing model predictions with measured NO concentrations, typically in low or atmospheric pressure flat-flames [1–4]. The joint experimental/modeling (chemical kinetics) investigations can provide valuable NO prediction mechanisms, such as NOMecha2.0 [1]. The NO measurements also have been reported at high-pressure; either in a gas phase [5–8] or in diesel [9] and GDI engine sprays [10–12]. At high pressure, various interferences arise due to absorption line broadening and increase in interfering species density [6]. The

gas phase works [5–7] identify sources of absorption and fluorescence interferences arising from combustion products. Lee et al. [6] provided NO excitation and detection strategies to minimize these interferences. Besides the gaseous products, additional light attenuation can occur in a sooting environment, as in diesel engines. Verbiezen et al. [9] implemented a sophisticated attenuation correction through bidirectional LIF and absorption spectroscopy [13]. NO formation in an aeronautical n-heptane swirl-stabilized spray flame has been investigated in detail by Cooper and Laurendeau [14] at various pressures [15]. A recent study [16] reported NO measurement in a high pressure n-heptane spray flame that simulates a diesel-like jet. n-heptane was chosen by the authors [16] since it is generally used as a representative fuel in chemical kinetics modeling. Additionally, n-heptane is one of the surrogate fuels chosen by engine combustion network (ECN) [17]. A few investigations were primarily focused on the development of NO measurement techniques [18–20].

In most of these studies, NO concentration was measured using either laser-induced fluorescence (LIF) or laser-saturated fluorescence (LSF) [3, 18, 21] technique. The LIF technique can be applied to provide either 1D (line) or 2D (planar) measurement. Typically, line measurements have been used when the spectral resolution is desired [7, 9, 16]. Planar measurements are most suited when spatial structures are more desired than spectral or temporal resolution. Although the LIF signal is proportional to a probed species concentration, the quantitative deduction is not trivial. The fluorescence intensity also varies with temperature (Boltzmann fraction, quenching cross-section) and gas composition due to collisional quenching. Therefore, to

interpret the LIF signal, it is necessary to know both the temperature and gas composition. These additional quantities need to be measured simultaneously. In general, spontaneous Raman scattering is employed to measure species concentration, while Rayleigh scattering is used to measure temperature [22]. These techniques are well-established primarily in non-sooting gaseous flames. Implementation of such multi-scalar measurements is not only expensive but could augment the measurement uncertainties [23], owing to the propagation of uncertainty attributed to each technique. Furthermore, not all quenching species can be measured with Raman scattering [16], and thus requiring one to depend on adiabatic equilibrium calculation [16]. The LSF technique implemented by Cooper et al. [18] is considered to be insensitive to quenching, and thus eliminating the need to know the gas composition. Although LSF has so far [3] yielded in a valuable contribution, the spatial resolution is generally limited to a point or line due to the larger fluence requirement ($> 2\ J/cm^2$ [3]). Besides, the gas temperature must be known to deduce NO concentration. In a sooting flame, LSF will lead to a strong interference from laser-induced incandescence (LII) due to high fluence.

Additionally, various challenges (in LIF and LSF) originate from the two-phase nature of spray flame itself. The Mie scattering noise from the droplets is several orders larger than the NO fluorescence. Furthermore, fluorescence from unburned hydrocarbons (UHC) and polycyclic aromatic hydrocarbons (PAH) [18] introduces severe interference. Consequently, only a few research groups [9–12, 14, 16] have reported quantitative NO measurements in spray flames. These past works focused on spray flames at elevated pressure, while

NO concentration at atmospheric pressure is scarce. At atmospheric pressure, the existence of larger spray droplets severely increases Mie scattering noise. In a sooting spray flame, besides the PAH interference, the LII and scattering from soot particles pose additional difficulties.

In view of these challenges, accurate measurements in well-defined target flames are valuable for the modeling community. The most recent workshop on Turbulent Spray Combustion [24] has established three well-documented experiments that are appropriate for model validations. The database generated by CORIA Rouen spray burner (CRSB) group has been recognized as one of the candidates along with the Sydney [25] and Cambridge [26–28] burners. The CRSB database includes a wide range of quantities, namely: spray shadowgraphy, droplet size and temperature, flow and droplet velocities, flame-structure, and ignition probability map.

The primary objective of this investigation is to report quantitative planar NO concentration in two-phase atmospheric spray flame, thereby expanding the CRSB database. Additionally, a novel diagnostic and correction strategy to account for varying temperature and gas composition LIF dependencies is demonstrated. The NO formation within the spray flame structure is also discussed. Thus, the present work contributes to the spray combustion field on three following fronts: *i*) the database for model validations, *ii*) quantitative NO measurement strategy, and *iii*) identification of the NO formation zones.

2. Experimental methods

2.1. Burner

A lifted spray flame was stabilized on an unconfined atmospheric pressure CRSB facility. The burner geometry is detailed in previous works [29, 30]. *n*-heptane in the liquid phase was injected through a simplex injector (Danfoss, 1.35 kg/h, 80^o hollow cone). A non-swirling air coflow was issued around the fuel injector through an annulus opening ($d_o = 20\ mm,\ d_i = 10\ mm$). Air and fuel flow rates were maintained using thermal and Coriolis mass flow controllers, respectively. The mass flow rate of air was 6 g/s, whereas liquid fuel was injected at 0.28 g/s rate, leading to a global equivalence ratio of 0.71. This flame condition has been selected earlier as a target case [29] considering the flame stability.

2.2. Laser diagnostics

The simultaneous OH/NO PLIF system was set-up to image the average NO concentration and flame front. A total of 1500 simultaneous OH/NO PLIF image pairs were acquired at 3.3 Hz rate to tackle statistical biases arising in turbulent spray flames [31, 32]. During the simultaneous OH/NO acquisitions in the spray flame, an additional emICCD camera (PI-MAX®4: 1024 EMB, Princeton Instruments) simultaneously images the NO-PLIF signal from a NO-seeded McKenna reference flame. This arrangement provides information on drifts in wavelength, energy, and spatial stability of the NO light-sheet throughout the experimental run. The OH and NO laser sheets were overlapped in space within 0.3 mm and were separated temporally by 300 ns. Both OH and NO PLIF cameras were gated to 100 ns with refer-

ence to the respective laser pulse. The cameras were aligned to image nearly identical field-of-view (FOV). Additionally, a pixel-by-pixel overlap between OH and NO images was achieved by applying a second-degree polynomial transformation using a calibration target. The FOV was 28.6 mm tall and 31 mm wide, with a magnification of 33 $pixels/mm$.

OH was excited by tuning the laser to $Q_1(6)$ line of $A-X(1,0)$ transition located near 283 nm, and the resulting fluorescence was collected around 310 nm. An Nd:YAG laser (Brilliant-B, Quantel) operating at second harmonics was used to pump a frequency-doubled dye laser (TDL90, Quantel) running with Rhodamine 590 dye to generate 283 nm. A $\sim$35 mm tall and $\sim$0.2 mm thick light-sheet was formed with a pulse energy of $\sim$8.5 mJ. The OH fluorescence was collected on an ICCD camera (PI-MAX®4: 1024f, Princeton Instruments) equipped with UV lens (100mm f/2.8, Cerco). The following set of filters were used: a narrowband 315 nm (15 nm bandwidth), UG11 and WG305 Schott. Such narrowband detection was necessary to suppress intense Mie scattering noise from fuel droplets and interference from PAH fluorescence.

NO was excited through $Q_1(29.5)$ transition of the $A-X(0,0)$ band at 225.12 nm (specified in vacuum) with the laser linewidth of 0.1 cm^{-1}. Thus, NO excitation at 225.12 nm involved multiple transitions, namely $Q_1(29.5)$, $R_2(25.5)$, $P_{21}(29.5)$, and $Q_2(31.5)$. Nevertheless, following the intensity dominance and for brevity we simply refer to these transitions as $Q_1(29.5)$ henceforth. The NO-LIF was collected from six $A-X(0,1)$ to (0,6) bands (at 235, 245, 257, 269, 282, and 297 nm, as marked in Fig. 1) to maximize the signal. The $Q_1(29.5)$ transition was selected based on LIF simulations (discussed in

Sec. 3.3). The $Q_1(29.5)$ transition was ensured by comparing experimental excitation spectrum with that of the LIFSim [33] just before the experimental campaign. Such precaution is necessary, since the LIF temperature dependence changes with transitions, and additionally the LIF intensity is highly sensitive to wavelength. At atmospheric pressure, due to the narrow linewidth of the excitation lines, 1 pm shift in wavelength could alter the NO signal by $\sim$6% from the peak value.

The NO-PLIF system consisted of a frequency-doubled Nd:YAG laser (YG980, Quantel) which pumps a frequency-tripled dye laser (Q-scan, Quantel) running LDS798 dye, ultimately generating 225.12 nm. The pulse energy at the burner axis measured $\sim$3.5 mJ. To reduce nonuniformity, the light-sheet was largely expanded, and only a central part was used. The resulting laser-sheet was $\sim$0.15 mm thick with an estimated mean fluence of 0.02 J/cm^2. Such a low fluence is necessary to reduce soot originated LII interference. For instance, 0.02 J/cm^2 fluence was used by Olofsson et al. [34] and Köhler et al. [35] to avoid LII effects in their elastic scattering and particle image velocimetry measurements, respectively. The LII signal appears at a typical threshold fluence of $0.05 - 0.10$ J/cm^2 [36], well-above the fluence used in our work. Additionally, in the present flame, soot generation primarily occurs outside the considered field of view (see Fig. 3). The use of low fluence also ensures that the NO-LIF is in the linear regime of laser fluence. The past works [2, 3] suggest NO-LIF linearity up to 1.5 J/cm^2 fluence.

The NO fluorescence signal was imaged on an emICCD camera (PI-MAX®4: 1024 EMB, Princeton Instruments) to ensure lower intensifier

noise. The LIF signal was collected in the $230 - 300$ nm range using five stacked filters, namely: two 224 nm long-pass edge filters (LP02-224R-25, Semrock), 300 nm and 350 nm short-pass filters (ZUS0300, ZUS0350, Asahi Spectra), and a UG5 Schott filter. This combination resulted in a complete elimination of Mie scattering (transmission of $2e{-}14$ @ 225 nm as shown in the inset of Fig. 1) from fuel droplets. The combined transmission curve of this filter stack along with the NO fluorescence bands is plotted in Fig. 1. The fluorescence spectrum is obtained using a LIF model (detailed in Appendix A) with $Q_1(29.5)$ transition at 225.12 nm in synthetic air at atmospheric pressure. The transmission values at the different fluorescence bands $A - X(0,1)$ to (0,6) are as follows: 0.05@235, 0.27@245, 0.44@257, 0.55@269, 0.62@282, 0.58@297 nm. The broadband ($230{-}300$ nm) detection strategy provides a higher signal; however, it also leads to interferences from other species (shown later in Fig. 8). Ideally, a narrowband detection near 235 nm would be suited to avoid broadband interference. However, a filter with high transmission at 235 nm and high rejection at the excitation wavelength (transmission $2e{-}14$ @ 225 nm) and larger wavelengths (>240 nm) was not available for the present measurements. Nevertheless, on a mean basis, the broadband interference can be eliminated by subtracting detuned signal as demonstrated subsequently in Sec. 3.4.1.

2.3. NO-LIF simulation

In a linear regime for an isolated transition, the LIF signal intensity S_f can be described [37, 38] as,

$$S_f \propto [\chi_{NO}/T] f_b(T) B[A/(A + Q(\chi_p, T))] \tag{1}$$

where χ_{NO} is the NO mole fraction, f_b is the Boltzmann fraction, B and A are the Einstein coefficients of absorption and spontaneous emission, respectively, Q is total quenching rate, and χ_p is the mole fraction of perturbing species. S_f can be expressed either on per NO molecule basis or per unit NO mole fraction. LIF intensity per molecule is denoted by S_{f^*}, while S_f per unit mole fraction is denoted by S_{f^+}, similar to [39]. The temperature and gas composition dependence of the LIF signal arises from the $f_b(T)$ and $Q(T, \chi_p)$ terms. The quenching rate is expressed as a sum over the collision partners,

$$Q = (P/k_b T) \sum_i \chi_i \sigma_i v_i \tag{2}$$

where k_b is the Boltzmann constant, χ_i and σ_i are the mole fraction and quenching cross-section of the i^{th} perturbing species, and v_i is the relative velocity between the probed and the i^{th} perturbing species. Thus, a quantitative concentration deduction needs appropriate corrections to account for varying LIF dependency with temperature and gas composition. Such correction requires the knowledge of spectroscopic data and experiment-specific parameters associated with LIF excitation and detection, which must be included in the LIF model.

A five-level LIF model [40] was developed along similar principles to those of Naik and Laurendeau [41]. The developed LIF model [40] accounts for overlapping transitions using the laser linewidth (0.1 cm^{-1}) value. A brief description of the present LIF model is provided in the Appendix A. The LIF simulations of our model [40] are in close agreement with that of the LIFSim [33] as shown in Fig. 2. The simulated S_{f^*} corresponds to the $Q_1(29.5)$ transition at 225.12 nm in synthetic air at atmospheric pressure. Our LIF model contained five species for collisional quenching calculation, namely N_2,

O_2, Ar, CO_2, and H_2O. However, a few species with larger quenching cross-sections exist in the present spray flame (discussed in Sec. 3.3). To account for additional quenching, one needs to incorporate species-specific spectroscopic parameters and modify the LIF model. Such modification would be flame dependent (quenching species). Instead, we implement a simple surrogate species approach, which enables quick calculation without any substantial modification to the existing LIF model.

The approach involves mole fraction (χ) substitutions weighted by respective quenching cross-section (σ) obtained from [42]. We consider a set of species in quenching calculations based on the combined relevance of χ (obtained from LES data) and σ. Paul et al. [42] provides collisional quenching rate for a large number of perturbing species. The authors [42] have identified six classes of collision partners. Species in a particular class tend to have identical trends in quenching cross section with temperature, $\sigma(T)$. Based on this classification and $\sigma(T)$ trends, we associate replacing species to a specific surrogate available in the present LIF model. Consequently, the mole fraction of a replacing species χ_r is σ weighted and then added to an ideal surrogate χ_s as, $\chi_s^{'} = \chi_s + \chi_r(\sigma_r/\sigma_s)$, where $\chi_s^{'}$ is the revised mole fraction of a surrogate. In this manner, N_2 is surrogate for CO, which leads to a revised mole fraction as follows, $\chi_{N_2}^{'} = \chi_{N_2} + \chi_{CO}(\sigma_{CO}/\sigma_{N_2})$. Similarly, H_2O is surrogate for C_2H_2 and C_2H_4, and finally Ar is surrogate for C_7H_{16}, CH_4 and H_2. Thus, revised mole fractions indirectly account for quenching by additional species unavailable in the LIF model. Total quenching rate (evaluated using Eq. 2) of a surrogate mixture is within $\pm 1\%$ that of the original gas composition over a region of interest in the present spray flame. This verification

ensures a reliable deduction of NO concentration despite the simplification. Various uncertainty sources in NO concentration deduction are discussed in Sec. 3.4.2.

3. Results and discussion

3.1. Flame structure

Figure 3 shows the spray flame photograph along with an instantaneous OH-PLIF image. The photograph shows a blue part near the leading edge, while the downstream portions exhibit yellow luminosity associated with the soot presence. Soot and soot-precursors (PAH) can interfere with NO measurements. Mie scattering from fuel droplets can be observed around the traversing laser beam. The OH-PLIF image within the region of interest is shown on the right. Mie scattering noise from fuel droplets and interference from PAH are nearly eliminated owing to the narrowband filter. The double flame structure containing a thin inner OH layer (B1) and a relatively thick outer OH layer (B2) is observed, which typically exists in spray flames [43, 44]. The outer flame branch (B2) is less wrinkled and without any local extinctions due to lower turbulence levels as reported in the previous study [45]. The inner reaction zone (B1) is highly wrinkled with frequent local extinctions caused by intense turbulence [45]. Mechanisms of local extinction are elucidated by Verdier et al. [30] through droplet-turbulence-flame interactions. The local extinction is primarily attributed to intense strain rate. Extinction at the flame leading edge (S) is attributed to the heat transfer between the flame and droplets. The effect of droplets on the flame structure can be noticed by observing small holes occurring locally within the OH layer

(Fig. 3). Few of these droplets even appear to escape the outer flame branch (B2). Although no extinction is observed in the B2 branch, drop in local heat release rate has been suggested [30].

The OH layer along the inner branch appears thinner than the outer branch. Based on the OH-PLIF signature, a previous study [43] suggested that the flame-structure of the inner branch shared predominantly diffusion-like characteristics, while Marley et al. [44] argued that the inner branch transitions to a partially premixed structure downstream of the leading edge. The recent experimental-simulation joint investigation provides a quantitative flame-index approach [45] that led to definitive conclusions. The flame-index based on the fuel and oxidizer concentration gradient differentiates the mode of combustion such that the index is positive for the premixed flame and negative in the non-premixed flame. Since NO concentration is highly sensitive to the flame structure and combustion mode, we revisit the relevant findings in [45]. The inner branch B1 was shown to possess a composite structure with two closely spaced reaction zones: a fuel-lean premixed (B1-P) and a non-premixed (B1-D), as indicated in Fig. 3. This composite structure is the reason for the thin OH layer of the inner branch (B1). Combustion in the outer branch B2 occurs through a non-premixed mode, as substantiated by the flame-index [45]. The Zone-C is reported to be fuel-rich due to enhanced droplet evaporation.

3.2. NO-LIF Calibration

Flames with known concentrations of NO were stabilized on a water-cooled McKenna flat-flame burner (Holthuis & Associates) to calibrate the NO-LIF signal. A NO-seeded flame was also used to obtain the light-sheet

profile and flat-field, which were later used to correct the spray flame data. The gas mixture containing $CH_4/O_2/N_2/NO$ was issued through the 60 mm sintered porous plug. The core flow was surrounded by an annular shroud of nitrogen. All the flow rates were regulated by thermal mass flow controllers. The desired concentration of NO in the reactant was achieved by replacing part of the pure N_2 with the NO-doped N_2 gas. The mass flux ratio was kept constant at 0.125 $kg/m^2.s$ for all the seeding levels, resulting in a 10 cm/s bulk velocity. The base case (without NO seeding) flow rates were: 1.3 liters per minute (lpm) of CH_4, 3.3 lpm of O_2, and 12.4 lpm of N_2. Fuel-lean flame ($\phi = 0.8$) was used to reduce the seeded NO re-burn [19, 46]. Additionally, we calculate the *net* NO ($= nascent + seeded - consumed$) using burner stabilized non-adiabatic flame simulations with the Cantera software [47]. The recent well-validated NOMecha2.0 [1] mechanism was used. Since the NO concentration is highly sensitive to the temperature, the Cantera simulations were validated against the experimental data [48]. The authors [48] used similar McKenna burner, fuel, and mass flux as of the present work. Temperature measurements were performed at 15 mm above the burner along the axis using Coherent Anti-stokes Raman Scattering (CARS) technique with the estimated accuracy of $\pm 2.5\%$. The temperature difference between measurement [48] and simulation is found to be within 0.2% for $\phi = 0.8$, which validates the Cantera simulations.

The NO-PLIF measurements in the calibration flame were averaged over 200 laser shots. The detuned LIF signal was subtracted from the NO transition tuned signal. This subtraction accounts for background and any interference from other species. Next, a two-dimensional flat-field correction was

incorporated by assuming uniform concentration of NO within the field-of-view. Since the burner diameter is 60 mm, the NO concentration is expected to be uniform within the FOV (which is 31 mm wide). Flat-field correction accounts for the light-sheet profile, vignetting effects, and non-uniformity in the ICCD chip sensitivity. The signal in the corrected mean LIF image was spatially-averaged in the following region: $r = -15$ to $+15$ mm, and $z = 3$ *to* 30 mm, where r and z are the radial and axial coordinates with an origin located at the flame center. The spatially-averaged signal is plotted against the known *net* NO in Fig. 4. The calibration constants were derived from the linear fit. Excellent linearity between LIF intensity and the *net* NO concentration can be observed even up to 200 ppm. This calibration was performed just before the spray flame measurements, thus ensuring the identical LIF excitation (laser energy, wavelength, light-sheet profile) and detection (camera gain, gate width, lens) parameters. The measured LIF intensity (I_f) in spray flame is converted to a relative mole fraction χ^R_{NO} by applying McKenna calibration constants (C_1 and C_2) as, $\chi^R_{NO} = C_1 I_f + C_2$. The constant C_2 was retained although negligible as evidenced from Fig. 4. The deduced mole fraction is relative since the temperature and gas composition in the calibration flame are different than in the spray flame. We incorporate a LIF temperature-quenching correction to obtain absolute mole fraction as described subsequently.

3.3. LIF temperature-quenching dependence

The quantitative deduction of NO concentration from the LIF signal requires the knowledge of temperature and species concentration (at least major quenching species) throughout the field. Such planar simultaneous

measurements of species and temperature are not always feasible, and may introduce additional uncertainty as demonstrated in [23]. Therefore, we use temperature and species data obtained from LES performed at CERFACS using AVBP solver (www.cerfacs.fr/avbp7x). Sub-models for gas and liquid phases were the same as in [45], however, with an analytically reduced chemistry (ARC) model for n-heptane oxidation [49]. The ARC model allows access to the OH and other major NO-LIF quenchers such as C_2H_2 and C_2H_4, consequently enhancing the LIF quenching correction. A previous study [45] compared the LES results against the experimental data. The simulated and experimental mean flame-structures are compared in Fig. 5 to verify the agreement between simulation [45, 49] and present experiment.

Simulated OH mole fraction is averaged over 15 ms time due to limited computational resources, whereas the experimental OH-PLIF images are averaged over 1500 time-independent realization obtained at 3.3 Hz rate. Experiments were performed at two heights, and the data in overlapping regions is averaged. Few differences are observed between the experiment and simulation: i) the lift-off height of simulated OH is 18 mm, while experiment shows 25 mm, ii) the flame branch B2 appears to have a larger radial spread than the experimental observation, probably due to a limited radial computational domain (130 mm radius). The difference in lift-off height is likely due to the evaporation model implemented in the simulation and an asymmetry in the experimental flame-base ($\sim$1 mm). Despite these differences, a certain similarity is observed. For instance, the simulated flame-structure within $z = 18 - 50$ mm resembles that of the experimental one, but in the $z = 25 - 76$ mm range. Thus, we consider LIF simulations within

$z = 22 - 50\ mm$. Radial profiles of major species and temperature are extracted at seven axial locations. Figure 6 shows the profiles of the primary NO-LIF quenching species along with the temperature at $z = 30\ mm$. As stated earlier in Sec. 2.3, only species with the combined relevance of concentration and scattering cross-section are considered. NO is primarily formed in the post-flame zone between B1 and B2 branches (region C) and along the outer region of the B2 branch. Therefore, for LIF simulations, the profiles are radially restricted within two flame branches B1 and B2, conditioned to OH-local peaks as marked by the vertical lines in Fig. 6. Additionally, such conditioning facilitates the radial mapping of simulated NO fluorescence dependence to the experimental NO data, where OH-PLIF enables identical conditioning. The mapping procedure is detailed subsequently. The simulated fluorescence per unit mole fraction of NO (S_{f+}) are plotted in Fig. 7 by utilizing the LES temperature and gas composition at various heights. The simulated fluorescence spectrum is integrated by taking into account the filter transmission presented in Sec. 2.2. The S_{f+} profiles of the spray flame are normalized using the simulated LIF intensity at the McKenna calibration flame condition. The species and temperature for the calibration flame are obtained through Cantera simulation detailed in Sec. 3.2.

We have simulated NO-LIF profiles with six different transitions (corresponding to 224.82 [19], 225.12, 225.22, 225.58 [14], 226.03 [50], and 226.103 nm), which were chosen based on the past works and LIF yield. For brevity, we report results for two transitions. Figure 7a shows LIF dependence for the commonly used 226.03 nm wavelength [2, 6, 7, 9, 50–52] that excites $P_1(23.5),\ Q_1 + P_{21}(14.5),\ Q_2 + R_{12}(20.5)$ transitions. This scheme was orig-

inally optimized to reduce O_2-LIF interference at elevated pressures [19, 50]. However, in the present atmospheric pressure flame, a strong temperature-quenching sensitivity is observed from Fig. 7a. S_{f+} varies both axially (z) and radially (r) by a factor of nearly two. Thus, the use of 226.03 nm excitation will result in a significant uncertainty in the present flame. Figure 7b shows fluorescence dependence for $Q_1(29.5)$ transition at 225.12 nm. This transition results in a fairly low temperature-quenching sensitivity compared to the other six candidate transitions. Additionally, $Q_1(29.5)$ transition provides access to a neighboring detuning domain ($225.098-225.106$ nm), which facilitates the collection of background signal. Note that the radial domain of S_{f+} curves varies with height (see Fig. 7a) due to the change in distance between the B1 and B2 branches. Thus, for appropriate comparison the S_{f+} curves are scaled over a fixed representative radial range in Fig. 7b. The scaled curves are well-collapsed and the axial S_{f+} variation is primarily within $\pm 5\%$. This axial variation is neglected, and a mean S_{f+} curve (S_{f+}^{m-u}, *mean* derived from *unconditionally* time-averaged data) is deduced. Since the LIF simulations are performed using time-averaged species and temperature (obtained from LES), the flame fluctuations can cause errors in S_{f+} near the flame edges. Therefore, we also evaluate the conditional average by evaluating the S_{f+} curves using instantaneous LES data at various axial stations. The axial mean curve for each instant (time delay) is deduced in the same manner as of Fig. 7b. The data processing steps are detailed in Appendix C.1. Instantaneous concentration profiles at a certain height are used to estimate LIF dependence (S_{f-h}). S_{f-h} at seven axial stations in $z = 22$ to 50 mm region are evaluated. S_{f-h} curves are radially mapped to a fixed

range to enable conditional axial-averaging. The axial variation of instantaneous S_{f+} is primarily within $\pm 10\%$. The axially-averaged instantaneous S_{f+} curves are evaluated for 15 instants (S_{f+}^{m-1},...,S_{f+}^{m-15}) and plotted in Fig. 7c in gray. The instant-to-instant variation of S_{f+}^{m-i} is only $\pm 5\%$ around the mean. Next, the instantaneous curves are averaged to provide the conditional mean, S_{f+}^{m-c} represented in green in Fig. 7c. For a reference, S_{f+}^{m-u} is also plotted in red (same as in Fig. 7b). There is a close agreement between conditional and unconditional curves, except near the inner flame branch where strong fluctuations are observed. In other regions, S_{f+}^{m-c} almost overlaps with S_{f+}^{m-u}. Nevertheless, we only use the conditional mean curve, S_{f+}^{m-c} to correct the radial LIF temperature-quenching dependence. The spray flame LIF dependence is normalized with that of McKenna calibration flame as, $S_{f-N}^{m-c} = S_{f+}^{m-c}/S_{f+}^{McK}$. Finally, the relative mole fraction obtained from the calibration is converted to absolute concentration as, $\chi_{NO} = \chi_{NO}^{R}/S_{f-N}^{m-c}$.

Recall that the S_{f+}^{m-c} is conditioned on radial locations of B1 and B2 branches from LES data. In Fig. 7c, S_{f+}^{m-c} curve is radially scaled to a fixed representative range. With regards to experiment, the radial locations of B1 and B2 vary: 1) across simulation and measurement, 2) with height, and 3) between instant-to-instant. These spatial variations need to be accounted before applying the LIF dependence correction S_{f+}^{m-c}. The following mapping procedure is adopted. For a given instantaneous NO image, at each axial location, radial locations of B1 and B2 are determined from the corresponding OH image. S_{f+}^{m-c} is then spatially mapped (translation, scaling) to match the radial domain and resolution of experimental B1-B2. The procedure is repeated at all axial locations (pixel-by-pixel) over the entire domain. The

data reduction steps are detailed in Appendix C.3. In this manner, the mapping procedure accounts for spatial differences between simulated and experimental flame structures on the instantaneous-basis. Recall, we use the single axially-averaged S_{f+}^{m-c} dependence curve over the entire domain. Relevant errors due to the simplifications are accounted in the uncertainty estimate (Sec. 3.4.2). This novel correction strategy enables quantitative deduction of the LIF signal with a reduced uncertainty despite the differences in LES data and experiments.

3.4. NO concentration deduction

3.4.1. Interference in NO-LIF

The NO-LIF measurements are reported to have various sources of interference, especially at elevated pressures [6, 9, 16]. Although the present measurements are at atmospheric pressure, other sources of error may appear. The Mie scattering from droplets was completely eliminated through two sharp-edge filters (Sec. 2.2). Broadband interference was anticipated due to fuel-rich and non-premixed region of the flame. Thus, the NO-detuned (@225.103 nm) LIF measurements were performed in addition to the NO transition-tuned LIF acquisitions. A total of 500 detuned images were acquired. Figure 8 shows tuned and detuned mean signals intended for NO-LIF along with the mean flame contour. The flame contour is defined by a mean progress variable such that $\bar{c} = 0$ in a fresh gas and 1 in the post-flame zone. A region enclosed by the OH-centerline (nearly aligned to local OH peaks of B1 and B2 branches) was extracted from each instantaneous OH-PLIF image. In the case of local extinctions within the B1 branch, the flame segments were connected to the nearest neighbor. The 1500 instances were averaged

to obtain a mean progress variable map. The data reduction procedure is detailed in Appendix B. The contours plotted in Fig. 8 indicates $\bar{c} = 0.3$ (solid) and 0.9 (dotted) fronts extracted from Fig. B.11h.

As observed in Fig. 8b a significant interference exists. The detuned LIF signal measures ∼57% as of the NO transition-tuned signal. This is not surprising considering the fuel-rich environment (Zone-C), deep-UV excitation (225 nm), and broadband LIF collection ($230 - 300$ nm). Note that, the fuel-lean methane/air calibration flame does not contain such a significant interference. The detuned signal at 200 ppm NO seeding measures only ∼3% that of the tuned signal. Thus, the interference in the spray flame (Fig. 8b) is most likely attributed to fluorescence arising from PAH or UHC [18]. The PAH absorption and fluorescence spectral range provided by Bejoui et al. [53] suggests that the present NO excitation/detection scheme is susceptible to interference from one to two ring PAH. The radial distribution of detuned signal resembles that of the simulated C_2H_2 profile shown in Fig. 6. The PAH growth has been linked [54] to the pyrolysis of acetylene (C_2H_2). Thus, C_2H_2 qualitatively marks the PAH presence. We incorporate a correction by subtracting the mean detuned signal from that of the tuned data. The data reduction steps are listed in Appendix C.2. The detuned LIF signal (Fig. 8b) is primarily contained within the OH-fronts. However, beyond $z = 60$ mm, the detuned signal moderately spreads outside the mean flame front. Thus, the interference subtraction procedure for conditional averaging (discussed next) process is valid only till $z = 60$ mm. Consequently, the NO data beyond $z = 60$ mm is not retained.

As noted earlier from Fig. 7c, unconditional averaging in the presence of

strong flame fluctuations could lead to an artificial diffusion and thus becomes less representative. Therefore, we evaluate a conditional NO-PLIF average. The mean detuned LIF signal is subtracted from each instantaneous NO-PLIF image. Only the NO-PLIF signal bounded by the two flame branches B1 and B2 (derived from OH-PLIF) is considered, as of the simulated data shown in Fig. 6. The mean data is retained only at the locations where at least 200 conditional samples are available. The OH-PLIF data is also averaged conditionally. OH data only above a certain intensity threshold (8000 counts, which is ∼1/4th of the peak intensity) are considered. Similar to NO data, locations with at least 200 conditional samples are considered for the averaging.

3.4.2. Uncertainty estimation

Despite various corrections (light-sheet profile, LIF temperature-quenching dependence, detuned background, laser wavelength-energy drift) and experimental precautions (wavelength tuning, Mie scattering verification, laser drift monitoring), potential sources of uncertainty still remain. Therefore, uncertainties originating from calibration, experimental fluctuations, and LIF temperature-quenching dependence are estimated as follows.

1. Calibration: *a*) In the calibration process error in the NO concentration arises from uncertainty in the amount of NO doped in N_2 gas, which is ±2%. *b*) Uncertainty in gas mixture preparation associated to the uncertainty in mass flow rates is estimated to be ±2%. *c*) Uncertainty in net NO prediction is estimated as ±2%, since calculations are performed using well-validated NOMecha2.0 mechanism and temperature is verified against DLR experimental data. *d*) Another contributing source is the

random fluctuation in the LIF signal due to flow fluctuation, shot-to-shot laser beam profile and energy variations, and ICCD camera noise. This is estimated to be ±6% in a laminar McKenna flame by considering standard deviation ($S.D.$) and number of samples ($N = 200$) as $2S.D./\sqrt{N}$ (95% confidence interval). Thus, the combined calibration uncertainty from the above sources is estimated to be ±7%.

2. Fluctuations: *a*) Similar to the calibration flame, uncertainty in spray flame NO-tuned data due to shot-to-shot random fluctuations (in laser, camera, and flow) is estimated to be ±8% ($2S.D./\sqrt{N}$, with $N = 1500$). *b*) The NO-detuned signal (PAH-LIF) fluctuates from shot-to-shot, which can affect the mean-based PAH correction. To assess the effect of temporal PAH fluctuations, we deduce the root mean square (rms) of an area-averaged PAH signal in Zone-C ($r = 15 - 25\ mm$, $z = 30 - 40\ mm$). The rms measures 13% of the mean detuned signal. Consequently, uncertainty in mean PAH is 1.2% (95% confidence interval), which translates to 0.7% uncertainty in mean NO. Therefore, uncertainty in mean NO evaluation owing to the mean-based PAH subtraction is negligible.

3. LIF dependence: A significant uncertainty arises from the temperature and quenching dependence of LIF. *a*) Although we incorporate correction through LIF modeling, certain residual errors exist due to uncertainty in the LIF model, which is estimated to be ±16% based on past works [2, 52]. *b*) Additionally, simplifications such as surrogate species, and neglecting axial and instant-to-instant variations of LIF dependence (detailed in Sec. 3.3) lead to an estimated uncertainty of ±11%. *c*) Further contribution

arises from the use of simulated temperature and gas composition of spray flame. The spray flame simulations are validated against various measured parameters in the past [45]. Further, we utilize the data from recently improved simulation [49] that include additional species. However, the concentrations of NO-LIF quenching species are not known experimentally for absolute validation of LES data. Therefore, we performed a sensitivity analysis by perturbing the mole fraction of each LIF quenching species and the temperature. The simulated LIF signal varies only by ±4% to imposed ±10% perturbation in gas composition, whereas the LIF signal fluctuates by ±6% when the gas temperature is perturbed by ±10%. Based on this analysis, an uncertainty estimate of ±10% is associated with LES originating sources. Therefore, the combined LIF dependence uncertainty leads to ±22%.

4. Experimental sources: Three sources of experimental errors are discussed next. a) Drifts in laser wavelength, energy, and spatial profile over the measurement duration can lead to errors. During the spray flame campaign, the laser stability was monitored using the NO-LIF signal from a reference flame. The time-averaged light-sheet profile was spatially stable among different runs. However, the wavelength and energy drifted mildly over the measurement duration. If not accounted, this drift can lead to 10% error in NO as the entire experimental campaign lasted for an hour. Nevertheless, we correct the data to account for the drifts in energy and wavelength. Consequently, the error is negligible. b) Laser sheet extinction due to the droplet and PAH absorption may underestimate the NO. To minimize extinction of NO-LIF laser, a radial half of the flame ($r = 0$ to

40 mm) facing the laser-entrance side was imaged. Consequently, droplet-extinction and PAH-absorption effects are negligible at least for outer B2 branch. Within the Zone-C, primarily the benzene absorption is relevant [53] at 225 nm. Thus, the absorption by larger PAH is not appreciable. In the imaged region (z = 25 to 60 mm), the spray is dilute with fewer droplets in Zone-C as observed from the flame photograph in Fig. 3 where Mie scattering is highlighted by a traversing beam. Uncertainty from the steering of NO laser-sheet in the flame is not significant due to imaging of laser-entrance side of the flame and a short distance (< 20 mm) between B1-B2 branches. c) The NO-LIF signal can get trapped due to droplets and absorption by PAH. As discussed earlier, the droplet density is relatively lower in the imaged region. The NO-LIF emissions are dominant in the range of $225-270$ nm (Fig. 1), where primarily 1-2 ring PAH will contribute to the absorption [53]. In summary, drifts in NO excitation laser are accounted, while the laser extinction, beam steering, and fluorescence trapping could not be estimated precisely in the present spray flame from available data. Nevertheless, uncertainty from these sources is expected to be lower than the overall uncertainty.

Following the uncertainty propagation principle, the total uncertainty of $\pm 25\%$ is estimated in mean χ_{NO} measurement from accounted sources. The unaccounted sources (absolute species concentration from LES data, laser extinction, beam steering, and fluorescence trapping) are likely to augment the uncertainty. We provide a conservative estimate of $\pm 30\%$ overall uncertainty by assuming $\pm 15\%$ combined uncertainty from unaccounted sources.

Note that, the uncertainty in instantaneous χ_{NO} will be much larger.

The signal-to-noise ratio (SNR) for an instantaneous NO-LIF image is 3 in the NO-seeded (100 *ppm*) McKenna flame. The SNR was obtained by evaluating the mean to standard deviation ratio of the signal in a uniform NO concentration region (similar to [55]). In the spray flame, a uniform χ_{NO} region is not available to deduce the SNR. Instead, we evaluated the signal-to-background ratio (SBR). The SBR was estimated by comparing the spatially-averaged LIF intensity in a peak signal region with that of an area where NO is absent. The peak SBR in an instantaneous NO-LIF (detuned background subtracted) image is estimated to be 3.5 in the spray flame. This SBR value is comparable to SNR in the McKenna flame. The low SBR (or SNR) is attributed primarily to the intensifier noise, and lower NO concentration. With this SBR, the detectability limit is 15 *ppm* for an instantaneous image. Thus, we only report the mean, where the random noise reduces by a factor of square root of a number of samples. A typical detectability limit for mean NO is estimated to be about 1 *ppm* by considering locations with lower SBR.

3.4.3. NO concentration

Figure 9a shows conditionally averaged NO concentration (in *ppm*) along with the inner, outer, and centerline contours of the conditionally averaged OH-PLIF. The radial NO concentration profiles at two axial stations ($z = 40$ and 60 *mm*) are plotted in Fig. 9b along with the uncertainty band of $\pm 30\%$, as estimated in Sec. 3.4.2. The NO concentration adjacent to the flame branches (B1, B2) measures between $30 - 78$ *ppm*. This value is comparable to the measurements performed by Cooper and Laurendeau [15] who reported $\sim$33 *ppm* of NO in a swirl-stabilized (global $\phi = 0.9$) *n*-heptane/preheated-air spray flame at 2.09 *atm*. The present flame is markedly different in appear-

ance than that of the [15], due to atmospheric pressure and non-swirling unheated coflow of air.

χ_{NO} of ∼30 *ppm* is observed near the inner flame branch (B1) in Fig. 9a. The axial growth of NO measured from the leading edge (S) in the B1 branch is not appreciable (from 26 to 34 *ppm*). This can be explained through the temperature and residence time. The temperature in B1 is quite low (see Fig. 6), and thus non-thermal routes of NO formation may be dominant. Additionally, the lack of NO growth with a residence time (axial height) substantiates this argument. The flame-index [45] showed the existence of a lean-premixed reaction zone on the inner layer of the B1 (B1-P) branch, and a non-premixed reaction zone on the outer layer of B1 (B1-D). In turbulent fuel-lean flames such as B1-P, the nitrous oxide (N_2O) route of NO formation is suggested to be dominant [56]. In the B1-D non-premixed front, the Fenimore prompt mechanism [57] is likely to contribute to the NO production due to an abundance of fuel vapor in Zone-C. Thus, the B1 zone is likely to produce NO through the N_2O (in B1-P) and prompt (in B1-D) routes.

The NO concentration on the non-premixed outer branch (B2) measures consistently higher than that of the B1 branch. Near the leading edge (S), NO measures nearly the same (∼27 *ppm*) in both the (B1, B2) branches. A region of low NO concentration ($20 - 25$ *ppm*) is observed near $r = 16$ *mm*, $z = 30$ *mm*. Frequent extinction of the inner flame-branch is observed (through OH-PLIF, and in [30]) in this region. The local extinctions may lower the gas temperature due to the entrainment of cold reactant, consequently resulting in a low NO zone. Along the B2 branch, the local peak in NO appears to be well-correlated with the mean OH-centerline. Generally,

in a non-premixed reaction zone, the OH and temperature peaks occur about the same location. The NO formation along the B2 branch grows sharply with height (26 ppm at S to 75 ppm at $z = 60$ mm). This is attributed to the higher flame temperature in the B2 branch (Fig. 6) and to increased residence time. The flow velocity decays radially outwards and axially downstream [45]. Therefore, a sharp NO growth with an increase in residence time (downstream and radially outwards), along with the alignment of OH and NO peaks implies that the thermal mechanism of NO production is dominant in the B2 branch. The NO concentration between OH outer and centerline contours remains high, rather than being distributed uniformly about the OH-centerline. This is due to the existence of a fuel-lean (abundance of nitrogen and oxygen) region radially outward of B2, which consequently supports the high NO concentration, unlike that of the fuel-rich Zone-C.

4. Conclusions

The NO formation process in a dilute spray flame is investigated. Additionally, the quantitative NO measurement in a two-phase spray flame is presented along with the LIF correction strategies. A synergistic approach is demonstrated by utilizing simulated (LES) flame data to correct the experimental LIF measurements. Through NO-LIF simulations, the $Q_1(29.5)$ transition with a weak combined temperature-quenching sensitivity is selected. Furthermore, the temperature-quenching dependence correction is applied to the spray flame NO-LIF data. The broadband fluorescence from PAH is eliminated through detuned signal subtraction. This novel measurement and correction strategy led to a reasonably accurate (i.e., within $\pm 30\%$)

deduction of the mean NO despite the low concentration, two-phase flow, and fluorescence interferences.

As expected, the spatial distribution of NO is strongly affected by the spray flame-structure which exhibits various combustion modes and reaction zones. The NO concentration along the inner branch varies from 26 ($\pm$8) to 34 ($\pm$10) *ppm*, while the outer branch shows a sharp NO growth from 26 ($\pm$8) to 75 ($\pm$22) *ppm*. The slow growth and low concentration of NO in the inner branch suggest the prompt and nitrous oxide routes of NO production due to lower temperature and composite nature of the inner branch (containing adjacent fuel-lean and non-premixed reaction zones). A sharp NO growth along the outer pure diffusion branch is primarily associated with the thermal route owing to higher temperature and longer residence time. Thus, the NO formation is highly sensitive to the combustion mode, gas composition, residence time, and temperature. The present investigation contributes to a better understanding of NO formation in spray flames, to the development of NO measurement and correction strategies, and to the database in the dilute spray combustion area.

Acknowledgments

The authors are grateful for the financial support of Safran Aircraft Engines and the French National Research Agency (Industrial chair PERCEVAL). The authors thank Dr. E. Riber, Dr. B. Cuenot, Mr. F. Collin-Bastiani for providing the data on spray flame simulations performed at CERFACS, France by Dr. F. Shum-Kivan. The assistance of Mr. A. Vandel in burner installation and Mr. F. Corbin in software development is

gratefully acknowledged.

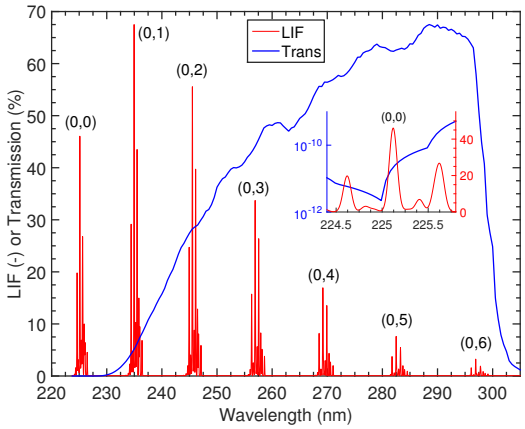

Figure 1: NO-LIF filter optical transmission along with the normalized NO fluorescence spectrum. The inset shows close-up near excitation wavelength, where the filter transmission is in log scale. Spectrum is simulated in synthetic air at atmospheric pressure using a LIF model [40]

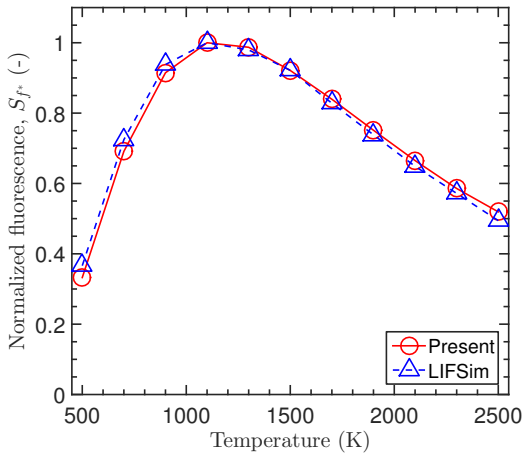

Figure 2: S_{f^*} from the present LIF model [40] compared with that of LIFSim [33] at different temperatures in atmospheric pressure synthetic air using $Q_1(29.5)$ excitation at 225.12 nm

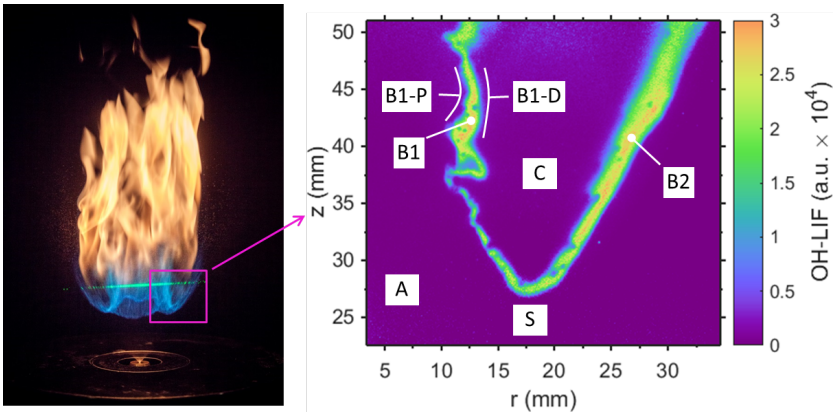

Figure 3: Flame photograph (1/1250 s exposure) and sample OH-PLIF image.

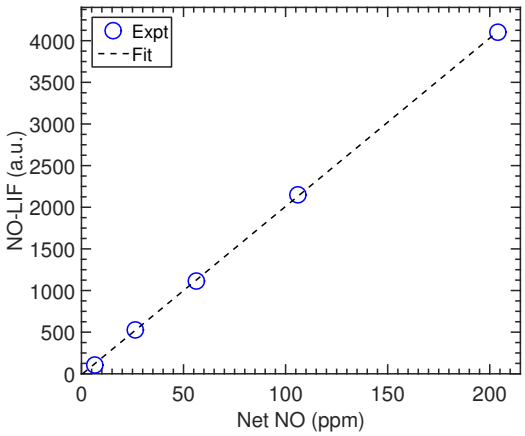

Figure 4: NO-LIF calibration in McKenna flat-flames.

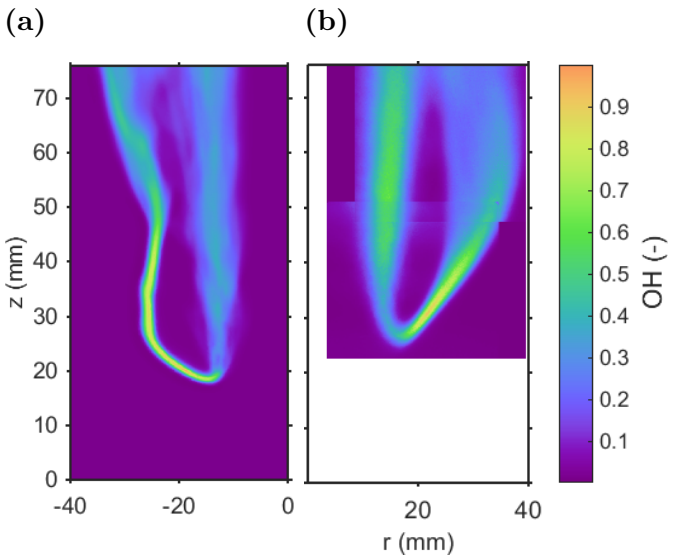

Figure 5: Mean OH: a) Normalized OH mole fraction obtained from simulation [45] using ARC chemistry [49], b) experimental OH-PLIF.

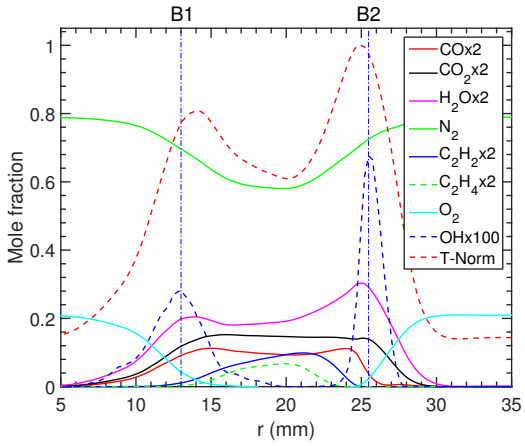

Figure 6: Simulated mean species and temperature at $z = 30\ mm$ extracted from Fig. 3(a). Temperature is normalized with peak (2151 K).

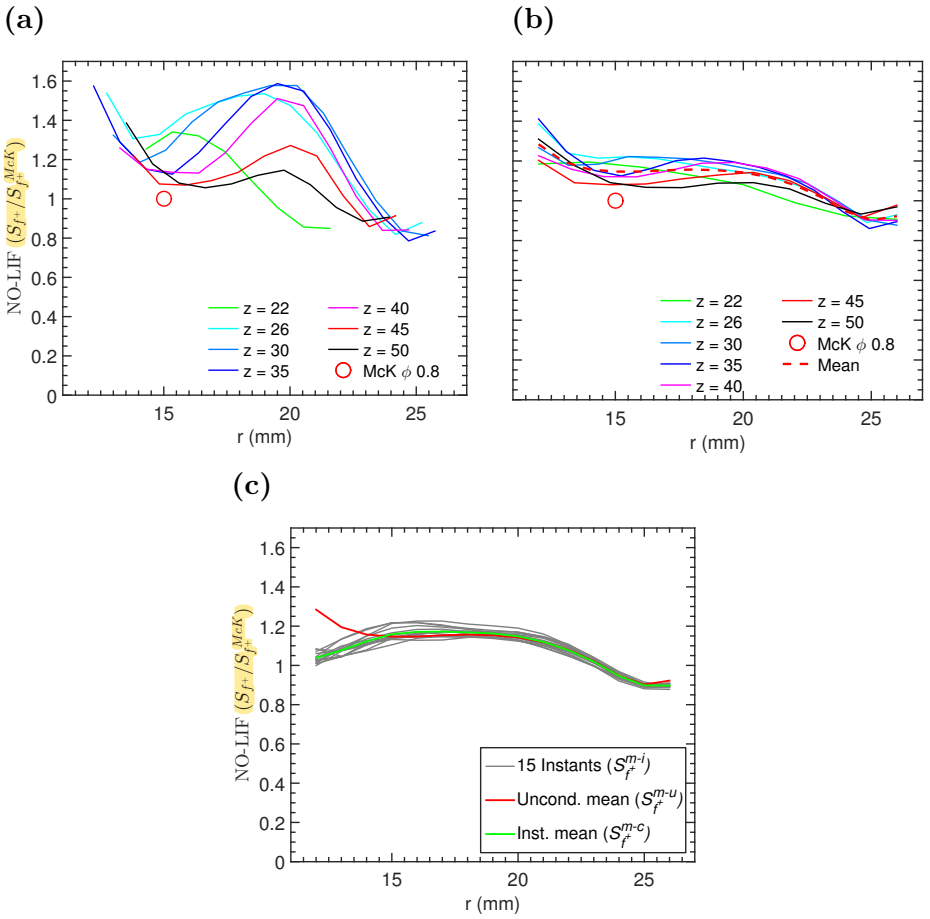

Figure 7: Simulated NO-LIF temperature-quenching dependence (S_{f^+}) in spray flame at various axial stations (z in mm) normalized by the McKenna calibration flame at two excitation wavelengths: (a) 226.03 nm, (b) 225.12 nm radially scaled, and (c) axially averaged LIF dependence of various instants along with the conditional and unconditional (time-averaged) mean with 225.12 nm.

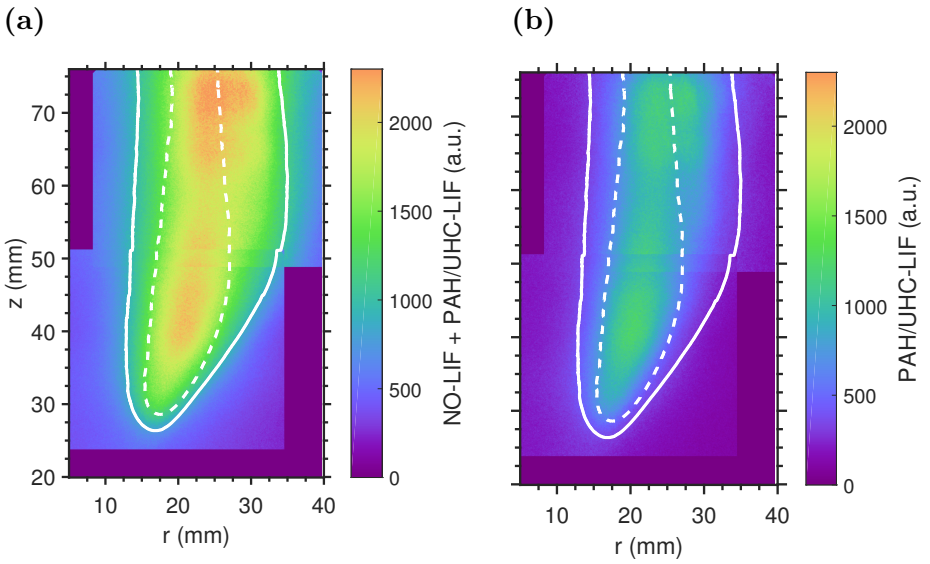

Figure 8: Mean LIF: (a) tuned to NO transition (b) detuned from NO transition, with the mean flame front $\bar{c} = 0.3$ (solid) and 0.9 (dotted).

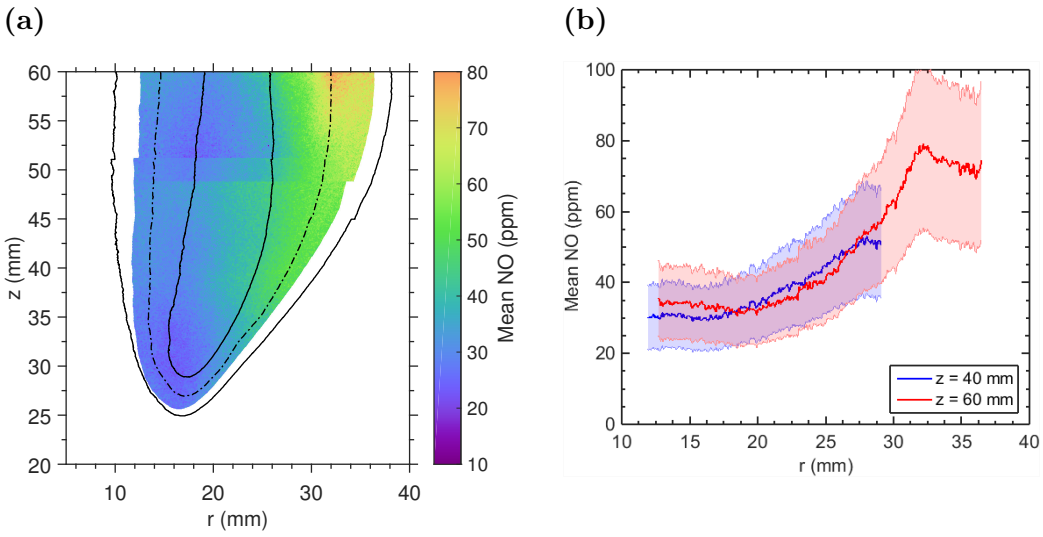

Figure 9: Conditionally averaged NO: (a) χ_{NO} with conditional mean OH contours and centerline, (b) χ_{NO} profiles with uncertainty bands.

Appendix A. NO-LIF model

The NO fluorescence dependence on temperature and species composition is calculated using a multi-level fluorescence model developed for quantitative NO concentration measurement in flames [40]. The essentials of the methodology are as follows. The excitation in NO-LIF usually occurs through a highly populated (0, 0) vibrational band. A photon in the range $224 - 227\ nm$ results in a resonant excitation from the $X^2\Pi(\nu'' = 0)$ state to the $A^2\Sigma^+(\nu' = 1)$ state. During this process, a strong non-resonant fluorescence from higher-vibrational bands of the $X^2\Pi$ state is observed which is often utilized in LIF imaging. To model this fluorescence scheme, a five-level model analogous to the one proposed by Naik and Laurendeau [41] is developed.

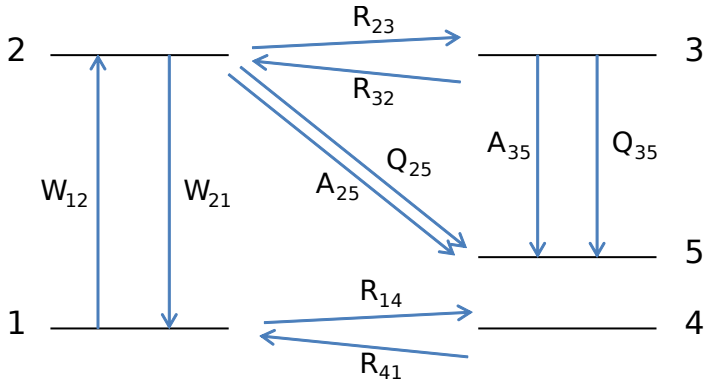

Figure A.10: Schematic of the five-level NO-LIF model

Figure A.10 illustrates the five-level model. The model includes rotational energy transfer (RET) as well as the energy back transfer from the excited level to the ground bath. The Levels 1 and 2 are laser-coupled, in which several rotational levels can be coupled via the finite laser linewidth. In

the lower state, RET from the bath Level 4 (ground state) to the Level 1 acts to replenish the laser-excited states, preventing the depletion of the population. The third level (in the upper state) represents the bath of the neighboring rotational energy levels which can exchange population with the Level 2 through RET. Finally, the laser-populated state (Level 2) and the upper state bath level (Level 3) decay to a fifth level which is not coupled with the initial level. This approach can be assimilated to an accurate model for energy transfer in NO for the following reasons. Firstly, the majority of the population of the excited states decay to vibrational and rotational states other than the initial pumped state. Secondly, the Vibrational Energy Transfer (VET) is slow compared to the characteristic time of laser excitation (i.e., the laser pulse duration). The following rate processes are considered in the present LIF model: *i*) Stimulated absorption and emission between the laser-coupled Levels 1-2 (W_{12} and W_{21}, respectively). *ii*) The spontaneous emission and collisional quenching between Levels 2-5 (A_{25} and Q_{25}) and Levels 3-5 (A_{35} and Q_{35}). *iii*) Rotational energy transfer between rotational bath Levels 2-3 (R_{23} and R_{32}) and Levels 1-4 (R_{14} and R_{41}).

The collisional quenching rates are calculated as a function of temperature using the correlations reported by Paul et al. [42]. The present LIF model contains five common combustion species, while the additional specific quenching species are modeled using a surrogate species approach as described in Sec. 2.3. A finite laser linewidth results in excitation of multiple overlapping rotational transitions. This is accounted by summing over the multiple transitions and through the integration of laser and absorption spectral profiles. Furthermore, the effect of spectral transmission of LIF col-

lection optics can be accounted by integrating the spectral transmission over the LIF spectrum.

Appendix B. Mean progress variable

This section briefly describes the methodology adopted to evaluate the mean progress variable using OH-PLIF. Figures B.11a to B.11c show sample OH-PLIF images along with the detected mid-contour (in magenta) representing the flame front. Such evaluation is not trivial due to local flame extinction, isolated flame islands, and convoluted flame front. The flame branches in a raw image are binarized by applying a threshold, which provides a thick region. The OH threshold of 8000 counts (∼1/4th of the peak intensity) is used based on values in gradient regions. Note that, we make use of OH-centerline which makes the deduction less sensitive to a threshold value. The centerline of the OH layer is detected by applying a RivMAP algorithm [58] that was originally developed to analyze the satellite imagery of a river. In case of local flame extinctions, OH-centerline is connected to the nearest flame segment as shown in Fig. B.11b. The isolated OH islands (observed in Fig. B.11c) are neglected by constraining start and end directions of the flame segment. The detected flame front for all of the 1500 instantaneous images is verified manually. Next, the region containing burnt gas is assigned a unity and the fresh gas is assigned to zero which provides binary images of progress variable as shown in Figs. B.11d to B.11f. The average of such 1500 images provides a mean progress variable which is plotted in Fig. B.11g. The similar procedure is repeated in the downstream field, and the mean progress variable map for the entire field ($z = 76\ mm$) is shown

in Fig. B.11h. This map is used in Fig. 8 to determine the spatial location of PAH interference relative to the flame front.

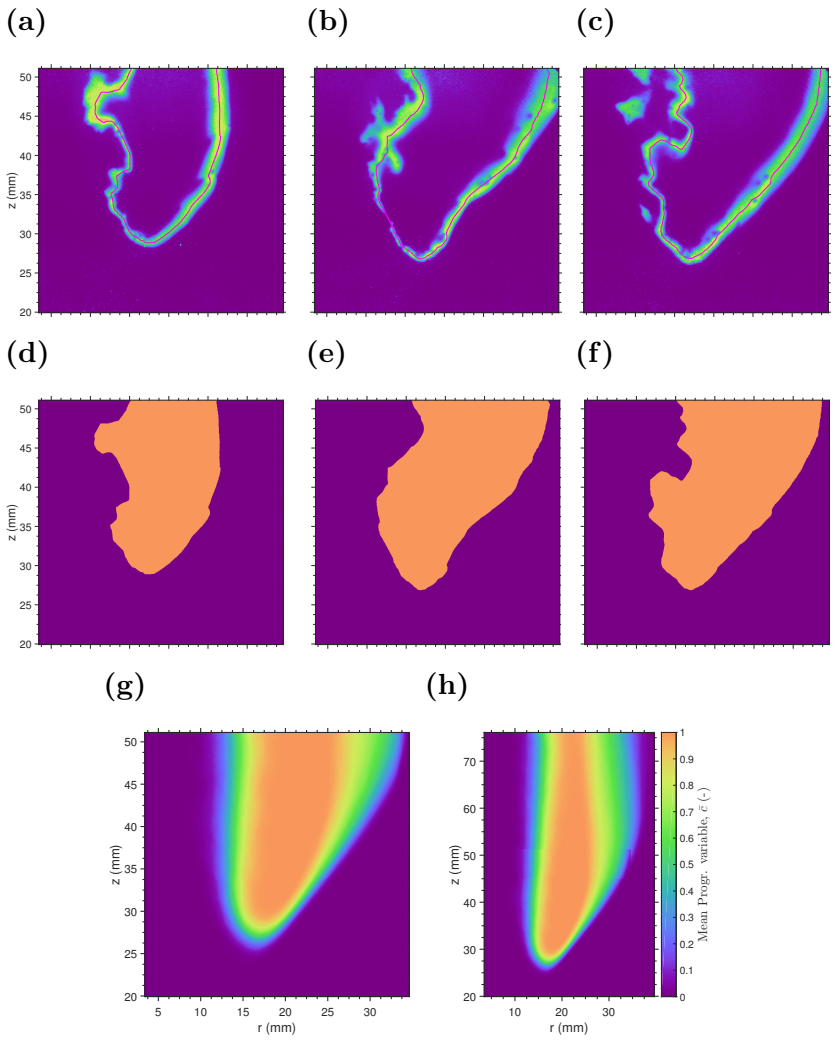

Figure B.11: Mean progress variable: (a)-(c): sample OH-PLIF images and detected flame front (magenta line), (d-f): corresponding binarized images, (g): mean progress variable, and (f) mean progress variable for entire field. The color bar for all the images are identical to that in (h).

Appendix C. Data processing steps

Appendix C.1. LIF temperature-quenching dependence

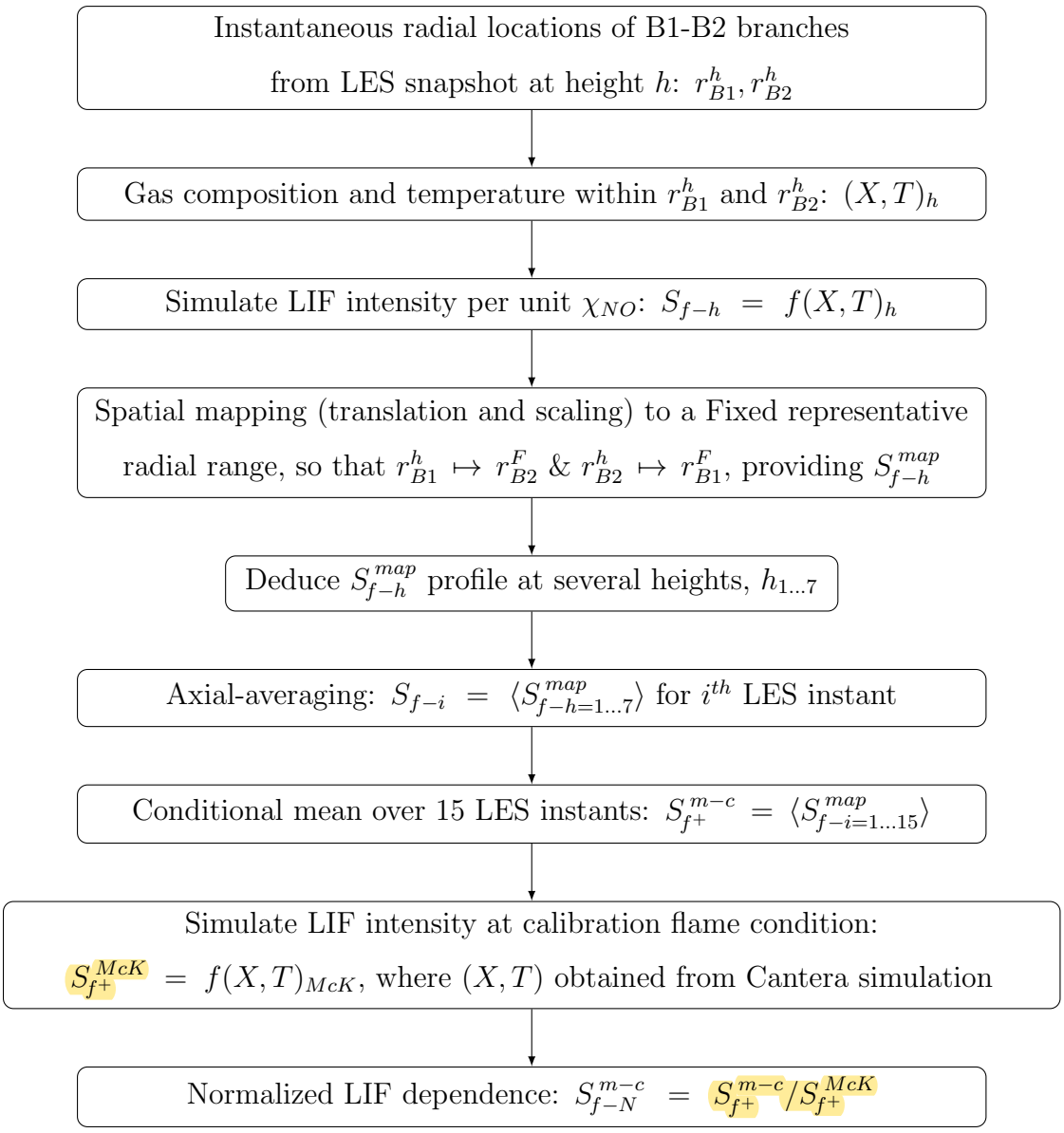

Figure C.12: NO-LIF temperature-quenching dependence.

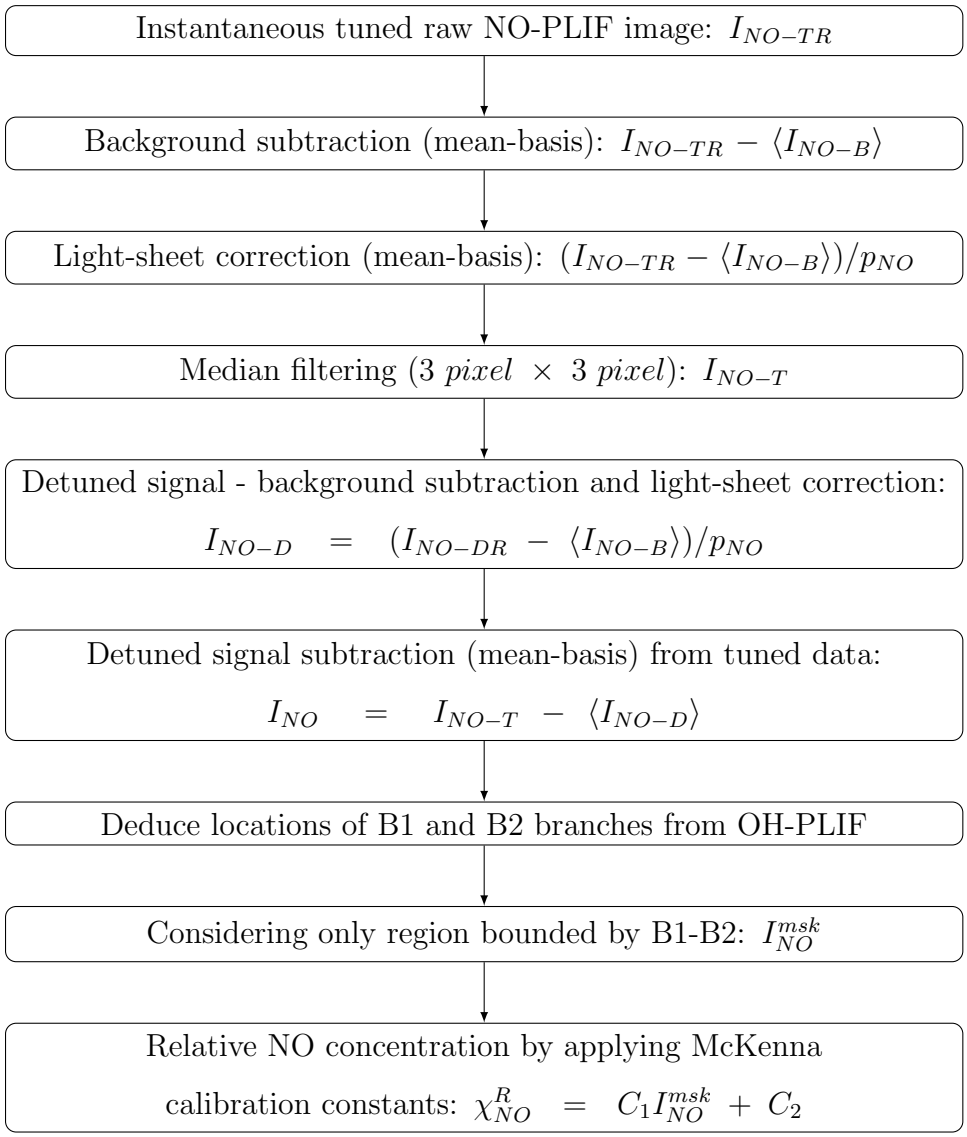

Figure C.13: Data reduction to obtain a relative NO concentration.

Appendix C.3. LIF temperature-quenching correction

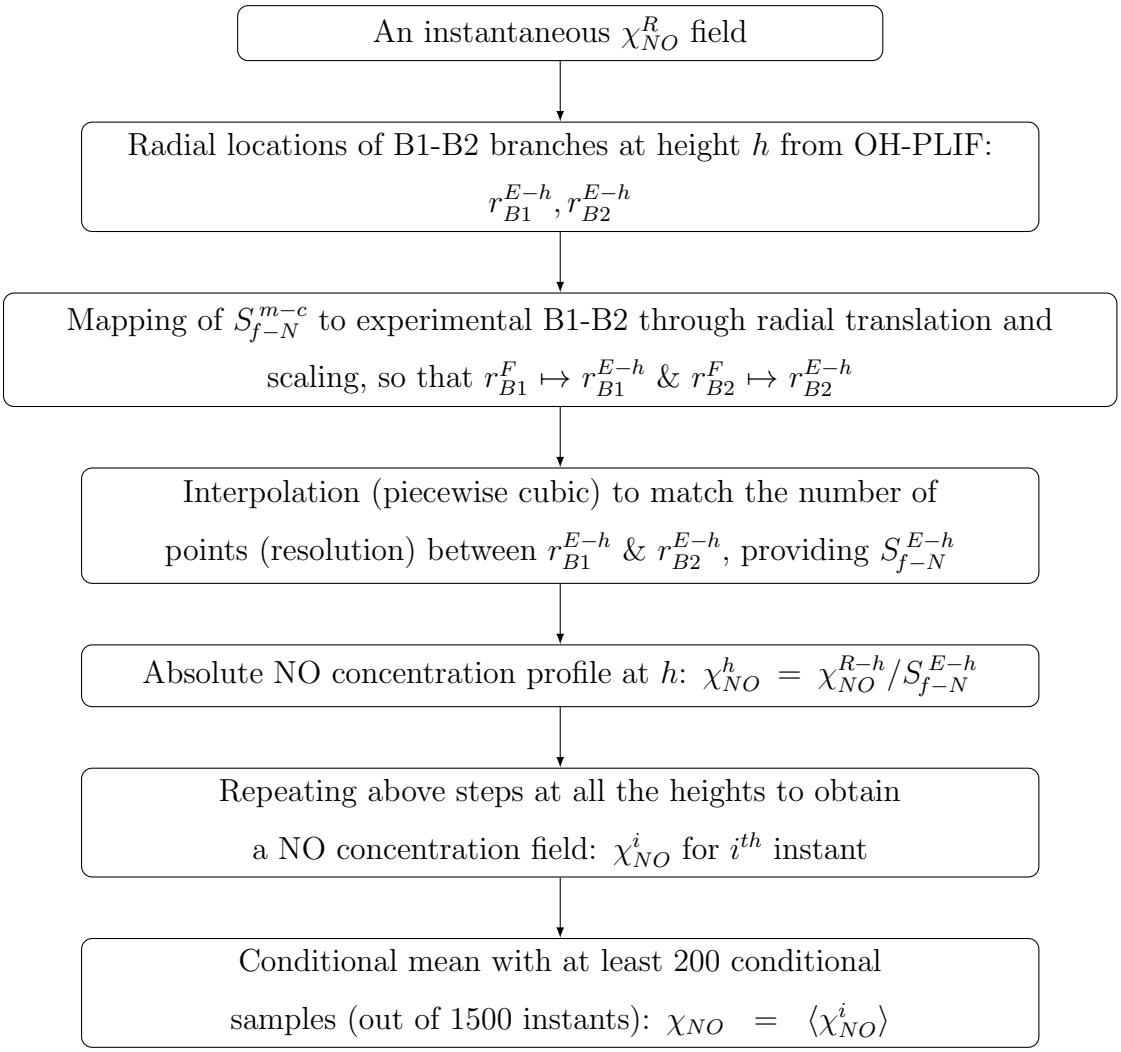

Figure C.14: LIF dependence mapping and correction.

References

[1] N. Lamoureux, H. El Merhubi, L. Pillier, S. de Persis, P. Desgroux, Modeling of NO formation in low pressure premixed flames, Combust. Flame 163 (2016) 557–575. doi:10.1016/j.combustflame.2015.11.007.

[2] A. B. Sahu, R. V. Ravikrishna, Quantitative LIF measurements and kinetics assessment of NO formation in H_2/CO syngas-air counterflow diffusion flames, Combust. Flame 173 (2016) 208–228. doi:10.1016/j.combustflame.2016.09.003.

[3] Z. Wang, Y. Zhou, R. Whiddon, Y. He, K. Cen, Z. Li, Investigation of NO formation in premixed adiabatic laminar flames of H_2/CO syngas and air by saturated laser-induced fluorescence and kinetic modeling, Combust. Flame 164 (2016) 283–293. doi:10.1016/j.combustflame.2015.11.027.

[4] R. Ravikrishna, N. M. Laurendeau, Laser-induced fluorescence measurements and modeling of nitric oxide in methane–air and ethane–air counterflow diffusion flames, Combust. Flame 120 (3) (2000) 372–382. doi:10.1016/S0010-2180(99)00101-7.

[5] W. G. Bessler, C. Schulz, T. Lee, D.-I. Shin, M. Hofmann, J. B. Jeffries, J. Wolfrum, R. K. Hanson, Quantitative NO-LIF imaging in high-pressure flames, Appl. Phys. B 75 (1) (2002) 97–102. doi:10.1007/s00340-002-0946-0.

[6] T. Lee, J. B. Jeffries, R. K. Hanson, Experimental evaluation of strategies for quantitative laser-induced-fluorescence imaging of nitric oxide in high-pressure flames (1–60 bar), Proc. Combust. Inst. 31 (2007) 757–764. doi:10.1016/j.proci.2006.07.090.

[7] J. Yoo, T. Lee, J. B. Jeffries, R. K. Hanson, Detection of trace nitric oxide concentrations using 1-D laser-induced fluorescence imaging, Appl. Phys. B 91 (3) (2008) 661–667. doi:10.1007/s00340-008-3030-6.

[8] R. Ravikrishna, S. V. Naik, C. S. Cooper, N. M. Laurendeau, Quantitative laser-induced fluorescence measurements and modeling of nitric oxide in high-pressure (6–15 atm) counterflow diffusion flames, Combust. Sci. Technol. 176 (1) (2004) 1–21. doi:10.1080/00102200490267331.

[9] K. Verbiezen, R. J. H. Klein-Douwel, A. P. Van Vliet, A. J. Donkerbroek, W. L. Meerts, N. J. Dam, J. J. Ter Meulen, Quantitative laser-induced fluorescence measurements of nitric oxide in a heavy-duty diesel engine, Proc. Combust. Inst. 31 (1) (2007) 765–773. doi:10.1016/j.proci.2006.07.061.

[10] W. G. Bessler, M. Hofmann, F. Zimmermann, G. Suck, J. Jakobs, S. Nicklitzsch, T. Lee, J. Wolfrum, C. Schulz, Quantitative in-cylinder NO-LIF imaging in a realistic gasoline engine with spray-guided direct injection, Proc. Combust. Inst. 30 (2) (2005) 2667–2674. doi:10.1016/j.proci.2004.08.123.

[11] U. Fissenewert, V. Sick, H. Pucher, Characterization of combustion and NO formation in a spray-guided gasoline direct-injection engine us-

ing chemiluminescence imaging, NO-PLIF, and fast NO exhaust gas analysis, in: SAE Technical Paper Series, SAE International, 2005. doi:10.4271/2005-01-2089.

[12] G. Suck, J. Jakobs, S. Nicklitzsch, T. Lee, W. G. Bessler, M. Hofmann, F. Zimmermann, C. Schulz, NO laser-induced fluorescence imaging in the combustion chamber of a spray-guided direct-injection gasoline engine, in: SAE Technical Paper Series, SAE International, 2004. doi:10.4271/2004-01-1918.

[13] K. Verbiezen, R. Klein-Douwel, A. Van Vliet, A. Donkerbroek, W. Meerts, N. Dam, J. Ter Meulen, Attenuation corrections for in-cylinder NO LIF measurements in a heavy-duty Diesel engine, App. Phy. B 83 (1) (2006) 155–166. doi:10.1007/s00340-006-2141-1.

[14] C. S. Cooper, N. M. Laurendeau, Parametric study of NO production via quantitative laser-induced fluorescence in high-pressure, swirl-stabilized spray flames, Proc. Combust. Inst. 28 (2000) 287–293. doi:10.1016/S0082-0784(00)80222-2.

[15] C. S. Cooper, N. M. Laurendeau, Quantitative measurements of nitric oxide in high-pressure (2–5 atm), swirl-stabilized spray flames via laser-induced fluorescence, Combust. Flame 123 (1-2) (2000) 175–188. doi:10.1016/S0010-2180(00)00165-6.

[16] T. Ottenwälder, C. Schulz, T. Raffius, H.-J. Koß, G. Grünefeld, K. A. Heufer, S. Pischinger, Quantitative nitrogen oxide measurements by laser-induced fluorescence in diesel-like n-heptane jets with enhanced

premixing, Combust. Flame 188 (2018) 250–261. doi:10.1016/j.combustflame.2017.09.035.

[17] L. Pickett, G. Bruneaux, R. Payri, Engine combustion network, https://ecn.sandia.gov/ (Accessed on 2019-01-29).

[18] C. S. Cooper, R. V. Ravikrishna, N. M. Laurendeau, Comparisons of laser-saturated, laser-induced, and planar laser-induced fluorescence measurements of nitric oxide in a lean direct-injection spray flame, Appl. Opt. 37 (21) (1998) 4823–4833. doi:10.1364/AO.37.004823.

[19] W. G. Bessler, C. Schulz, T. Lee, J. B. Jeffries, R. K. Hanson, Strategies for laser-induced fluorescence detection of nitric oxide in high-pressure flames. I. A-X(0,0) excitation, Appl. Opt. 41 (18) (2002) 3547–3557. doi:10.1364/AO.41.003547.

[20] C. Brackmann, J. Bood, J. D. Nauclér, A. A. Konnov, M. Aldén, Quantitative picosecond laser-induced fluorescence measurements of nitric oxide in flames, Proc. Combust. Inst. 36 (2017) 4533–4540. doi:10.1016/j.proci.2016.07.012.

[21] B. Li, Y. He, Z. Li, A. A. Konnov, Measurements of NO concentration in NH_3-doped CH_4+Air flames using saturated laser-induced fluorescence and probe sampling, Combust. Flame 160 (1) (2013) 40–46. doi:10.1016/j.combustflame.2012.10.003.

[22] R. S. Barlow, C. D. Carter, Raman/Rayleigh/LIF measurements of nitric oxide formation in turbulent hydrogen jet flames, Combust. Flame 97 (3-4) (1994) 261–280. doi:10.1016/0010-2180(94)90020-5.

[23] B. C. Connelly, B. A. V. Bennett, M. D. Smooke, M. B. Long, A paradigm shift in the interaction of experiments and computations in combustion research, Proc. Combust. Inst. 32 (1) (2009) 879–886. doi:10.1016/j.proci.2008.05.066.

[24] 6th workshop on measurement and computation of turbulent spray combustion, http://www.tcs-workshop.org/tcs6.html (Accessed on 2019-01-29).

[25] J. D. Gounder, A. Kourmatzis, A. R. Masri, Turbulent piloted dilute spray flames: Flow fields and droplet dynamics, Combust. Flame 159 (11) (2012) 3372–3397. doi:10.1016/j.combustflame.2012.07.014.

[26] R. Yuan, J. Kariuki, A. Dowlut, R. Balachandran, E. Mastorakos, Reaction zone visualisation in swirling spray n -heptane flames, Proc. Combust. Inst. 35 (2) (2015) 1649–1656. doi:10.1016/j.proci.2014.06.012.

[27] R. Yuan, Measurements in swirl-stabilised spray flames at blow-off, Ph.D. thesis, University of Cambridge (2015).

[28] R. Yuan, J. Kariuki, E. Mastorakos, Measurements in swirling spray flames at blow-off, Int. J. Spray Combust. 0 (0) (2018) 1–26. doi:10.1177/1756827718763559.

[29] A. Verdier, J. M. Santiago, A. Vandel, S. Saengkaew, G. Cabot, G. Grehan, B. Renou, Experimental study of local flame structures and fuel

droplet properties of a spray jet flame, Proc. Combust. Inst. 36 (2017) 2595–2602. doi:10.1016/j.proci.2016.07.016.

[30] A. Verdier, J. M. Santiago, A. Vandel, G. Godard, G. Cabot, B. Renou, Local extinction mechanisms analysis of spray jet flame using high speed diagnostics, Combust. Flame 193 (2018) 440–452. doi:10.1016/j.combustflame.2018.03.032.

[31] M. Allen, K. McManus, D. Sonnenfroh, PLIF imaging in spray flame combustors at elevated pressure, in: 33rd Aerospace Sciences Meeting and Exhibit, AIAA, 1995. doi:10.2514/6.1995-172.

[32] B. L. Upschulte, M. G. Allen, K. R. McManus, Fluorescence imaging of NO and O_2 in a spray flame combustor at elevated pressures, Symp. (Int.) Combust. 26 (2) (1996) 2779–2786. doi:10.1016/S0082-0784(96)80116-0.

[33] W. G. Bessler, C. Schulz, V. Sick, J. W. Daily, A versatile modeling tool for nitric oxide LIF spectra, 3rd Joint Meeting US Sec. Combust. Inst., Chicago, 2003, http://www.lifsim.com (Accessed on 2019-01-29).

[34] N.-E. Olofsson, H. Bladh, A. Bohlin, J. Johnsson, P.-E. Bengtsson, Are sooting premixed porous-plug burner flames one-dimensional? a laser-based experimental investigation, Combust. Sci. Technol. 185 (2) (2013) 293–309. doi:10.1080/00102202.2012.718006.

[35] M. Köhler, I. Boxx, K. Geigle, W. Meier, Simultaneous planar measurements of soot structure and velocity fields in a turbulent lifted

jet flame at 3 kHz, App. Phy. B 103 (2) (2011) 271. doi:10.1007/s00340-011-4549-5.

[36] H. Bladh, P.-E. Bengtsson, J. Delhay, Y. Bouvier, E. Therssen, P. Desgroux, Experimental and theoretical comparison of spatially resolved laser-induced incandescence (LII) signals of soot in backward and right-angle configuration, App. Phy. B 83 (3) (2006) 423. doi:10.1007/s00340-006-2197-y.

[37] A. C. Eckbreth, Laser diagnostics for combustion temperature and species, Vol. 3, CRC Press, 1996.

[38] P. H. Paul, J. A. Gray, J. L. Durant, J. W. Thoman, A model for temperature-dependent collisional quenching of NO $A^2\Sigma^+$, Appl. Phys. B 57 (4) (1993) 249–259. doi:10.1007/BF00325203.

[39] J. Koch, R. Hanson, Temperature and excitation wavelength dependencies of 3-pentanone absorption and fluorescence for PLIF applications, Applied Physics B: Lasers and Optics 76 (3) (2003) 319–324. doi:10.1007/s00340-002-1084-4.

[40] P. Gautier, Dosage des polluants NO et CO par imagerie de fluorescence induite par laser dans les écoulements réactifs, Ph.D. thesis, Normandie Université, France (2017).

[41] S. Naik, N. Laurendeau, Spectroscopic, calibration and RET issues for linear laser-induced fluorescence measurements of nitric oxide in high-pressure diffusion flames, App. Phy. B 79 (5) (2004) 641–651. doi:10.1007/s00340-004-1604-5.

[42] P. H. Paul, C. D. Carter, J. A. Gray, J. L. Durant Jr, J. W. Thoman, M. R. Furlanetto, Correlations for the NO $A^2\Sigma^+$ electronic quenching cross-section, Tech. rep., Sandia National Laboratories, SAND94-8237 (1995).

[43] A. Cessou, D. Stepowski, Planar laser induced fluorescence measurement of [OH] in the stabilization stage of a spray jet flame, Combust. Sci. Technol. 118 (4-6) (1996) 361–381. doi:10.1080/00102209608951986.

[44] S. K. Marley, E. J. Welle, K. M. Lyons, W. L. Roberts, Effects of leading edge entrainment on the double flame structure in lifted ethanol spray flames, Exp. Therm. Fluid Sci. 29 (1) (2004) 23–31. doi:j.expthermflusci.2004.01.009.

[45] F. Shum-Kivan, J. M. Santiago, A. Verdier, E. Riber, B. Renou, G. Cabot, B. Cuenot, Experimental and numerical analysis of a turbulent spray flame structure, Proc. Combust. Inst. 36 (2017) 2567–2575. doi:10.1016/j.proci.2016.06.039.

[46] P. A. Berg, G. P. Smith, J. B. Jeffries, D. R. Crosley, Nitric oxide formation and reburn in low-pressure methane flames, Proc. Combust. Inst. 27 (1998) 1377–1384. doi:10.1016/S0082-0784(98)80543-2.

[47] D. G. Goodwin, H. K. Moffat, R. L. Speth, Cantera: An object-oriented software toolkit for chemical kinetics, thermodynamics, and transport processes, http://www.cantera.org, version 2.3.0 (2017). doi:10.5281/zenodo.170284.

[48] P. Weigand, R. Lückerath, W. Meier, Documentation of flat premixed laminar CH_4/Air standard flames: temperatures and species concentrations, http://www.dlr.de/vt/Portaldata/29/Resources/dokumente/ch4_air_flames.pdf (Accessed on 2019-01-29).

[49] F. Shum-Kivan, Simulation des grandes echelles de flammes de spray et modélisation de la combustion non-prémélangée, Ph.D. thesis, Université de Toulouse, France (2017).

[50] M. D. Di Rosa, K. G. Klavuhn, R. K. Hanson, LIF spectroscopy of NO and O_2 in high-pressure flames, Combust. Sci. Technol. 118 (4-6) (1996) 257–283. doi:10.1080/00102209608951981.

[51] A. C. Lipardi, P. Versailles, G. M. Watson, G. Bourque, J. M. Bergthorson, Experimental and numerical study on NO_x formation in CH_4–Air mixtures diluted with exhaust gas components, Combust. Flame 179 (2017) 325–337. doi:10.1016/j.combustflame.2017.02.009.

[52] G. A. Chung, B. Akih-Kumgeh, G. M. Watson, J. M. Bergthorson, NO_x formation and flame velocity profiles of iso-and n-isomers of butane and butanol, Proc. Combust. Inst. 34 (1) (2013) 831–838. doi:10.1016/j.proci.2012.06.114.

[53] S. Bejaoui, X. Mercier, P. Desgroux, E. Therssen, Laser induced fluorescence spectroscopy of aromatic species produced in atmospheric sooting flames using UV and visible excitation wavelengths, Combust. Flame 161 (10) (2014) 2479–2491. doi:10.1016/j.combustflame.2014.03.014.

[54] H. Böhm, H. Jander, D. Tanke, PAH growth and soot formation in the pyrolysis of acetylene and benzene at high temperatures and pressures: Modeling and experiment, Symp. (Int.) Combust. 27 (1) (1998) 1605–1612. doi:10.1016/s0082-0784(98)80570-5.

[55] P. M. Allison, T. A. McManus, J. A. Sutton, Quantitative fuel vapor/air mixing imaging in droplet/gas regions of an evaporating spray flow using filtered rayleigh scattering, Optics Letters 41 (6) (2016) 1074. doi:10.1364/ol.41.001074.

[56] P. C. Malte, D. T. Pratt, The role of energy-releasing kinetics in NO_x formation: fuel-lean, jet-stirred CO-Air combustion, Combust. Sci. Technol. 9 (5-6) (1974) 221–231. doi:10.1080/00102207408960360.

[57] C. P. Fenimore, Formation of nitric oxide in premixed hydrocarbon flames, Proc. Combust. Inst. 13 (1) (1971) 373–380. doi:10.1016/S0082-0784(71)80040-1.

[58] J. Schwenk, A. Khandelwal, M. Fratkin, V. Kumar, E. Foufoula-Georgiou, High spatiotemporal resolution of river planform dynamics from Landsat: The RivMAP toolbox and results from the Ucayali river, Earth Space Sci. 4 (2) (2017) 46–75. doi:10.1002/2016EA000196.